1

Viscosity of erythritol and erythritol-water particles as a function of water activity: new

results and an intercomparison of techniques for measuring the viscosity of particles

Yangxi Chu[1,a], Erin Evoy[2,a], Saeid Kamal[2], Young Chul Song[3], Jonathan P. Reid[3], Chak K.

Chan[1] and Allan K. Bertram[2]

[1]School of Energy and Environment, City University of Hong Kong, 83 Tat Chee Avenue, Kowloon,

Hong Kong, China

[2]Department of Chemistry, University of British Columbia, 2036 Main Mall, Vancouver, BC, V6T

1Z1, Canada

[3]School of Chemistry, University of Bristol, Bristol, BS8 1TS, United Kingdom

[a]These authors contributed equally to this work.

Correspondence: Allan K. Bertram (bertram@chem.ubc.ca)

Abstract

A previous study reported an uncertainty of up to three orders of magnitude for the viscosity of

erythritol (1,2,3,4-butanetetrol) – water particles. To help reduce the uncertainty in the viscosity of

these particles, we measured the diffusion coefficient of a large organic dye (rhodamine B

isothiocyanate-dextran, average molecular weight $\sim$ 70,000 g mol^{-1}) in erythritol-water matrix as a

function of water activity using rectangular area fluorescence recovery after photobleaching

(rFRAP). The diffusion coefficients were then converted to viscosities of erythritol-water particles

using the Stokes-Einstein equation. In addition, we carried out new viscosity measurements for

erythritol-water particles using aerosol optical tweezers. Based on the new experimental results and

viscosities reported in the literature, we conclude the following: 1) the viscosity of pure erythritol

is 247^{+188}_{-107} Pa s (two standard deviations), 2) the addition of a hydroxyl (OH) functional group to

a linear C_4 carbon backbone increases the viscosity on average by a factor of 27^{+6}_{-5} (two standard

deviations), and 3) the increase in viscosity from the addition of one OH functional group to a linear

C_4 carbon backbone is not a strong function of the number of OH functional groups already present

in the molecule up to the addition of three OH functional groups, but the increase in viscosity may

be larger when the linear C_4 carbon backbone already contains three OH functional groups. These

results should help improve the understanding of the viscosity of secondary organic aerosol particles

in the atmosphere. In addition, these results show that the rFRAP technique, aerosol optical tweezer

technique, and bead-mobility technique give results in reasonable agreement if the uncertainties in

the measurements are considered.

Atmospheric
Measurement
Techniques
Discussions

39   1   **Introduction**

40   Secondary organic aerosol (SOA) is produced by the oxidation of volatile organic compounds

41   followed by condensation of oxidation products (Hallquist et al., 2009). SOA contributes

42   approximately 20 to 70% to the mass of fine aerosol particles, depending on location (Hallquist et

43   al., 2009; Jimenez et al., 2009; Kanakidou et al., 2005; Zhang et al., 2007). Despite the abundance

44   of SOA in the atmosphere, some physical and chemical properties of SOA remain poorly understood.

45   An example of one such poorly understood physical property is particle viscosity (Cappa and Wilson,

46   2011; Koop et al., 2011; Mikhailov et al., 2009; Perraud et al., 2012; Reid et al., 2018; Vaden et al.,

47   2011; Virtanen et al., 2010; Zobrist et al., 2008). The viscosity of SOA particles has implications for

48   predicting the size and mass distribution of SOA particles (Lu et al., 2014; Maclean et al., 2017;

49   Saleh et al., 2013; Shiraiwa and Seinfeld, 2012; Zaveri et al., 2014). Particle viscosity also

50   influences reaction rates (Berkemeier et al., 2016; Chu and Chan, 2017a; Chu and Chan, 2017b;

51   Gatzsche et al., 2017; Houle et al., 2015; Kuwata and Martin, 2012; Li et al., 2015; Liu et al., 2018;

52   Steimer et al., 2015; Wang et al., 2015; Zhou et al., 2012), photochemistry (Hinks et al., 2016;

53   Lignell et al., 2014; Wong et al., 2015), phase state (Baustian et al., 2013; Bones et al., 2012;

54   Shiraiwa et al., 2017), and ice nucleating ability of SOA (Bodsworth et al., 2010; Ignatius et al.,

55   2016; Ladino et al., 2014; Murray and Bertram, 2008; Schill et al., 2014; Wilson et al., 2012).

56   Particle viscosity also has implications for the long-range transport of pollutants (Bastelberger et al.,

57   2017; Shrivastava et al., 2017; Zelenyuk et al., 2012) and the optical properties of particles (Adler

58   et al., 2013; Robinson et al., 2014).

59

60   To improve the understanding of the viscosity of SOA particles, researchers have investigated the

61   viscosity of SOA in the atmosphere (Bateman et al., 2016; Bateman et al., 2017; O'Brien et al.,

62   2014; Pajunoja et al., 2016; Virtanen et al., 2010), the viscosity of SOA material generated in

63   environmental chambers (Grayson et al., 2016; Pajunoja et al., 2014; Renbaum-Wolff et al., 2013;

64   Song et al., 2015, 2016a; Virtanen et al., 2011; Ye et al., 2016), the viscosity of compounds identified

65   in SOA particles (Abramson et al., 2013; Bateman et al., 2015; Hosny et al., 2016), and the viscosity

66   of simple proxies of SOA material (Chenyakin et al., 2017; Marshall et al., 2016; Power et al., 2013).

67   In addition, researchers have investigated the dependence of viscosity on molar mass and the

68   number and type of functional groups (Grayson et al., 2017; Rothfuss and Petters, 2017; Song et al.,

69   2016b). For example, Grayson et al. (2017) investigated the dependence of viscosity on the number

70   of hydroxyl (OH) functional groups on a carbon backbone and found that viscosity increased, on

71   average, by a factor of 22 – 45 following the addition of an OH functional group to linear C_3, linear

72   C_4, branched C_5, and linear C_6 carbon backbones. However, the study by Grayson et al. revealed a

73   large discrepancy between the viscosity of erythritol (1,2,3,4-butanetetrol) measured with the bead-

74   mobility technique (Grayson et al., 2017) and measured with the aerosol optical tweezer technique

75   (Song et al., 2016b) at ≤ 25% relative humidity (RH). This led to uncertainties when predicting the

76   effect of adding OH functional groups to a linear C_4 carbon backbone on viscosity. This also led to

Atmospheric
Measurement
Techniques
Discussions

77 uncertainties regarding the viscosity of tetrols, which have been observed in ambient SOA particles

78 and SOA particles generated in environmental chambers (Claeys, 2004; Edney et al., 2005; Surratt

79 et al., 2006, 2010).

80

81 To help reduce the uncertainty in the viscosity of erythritol-water particles, we measured the

82 diffusion coefficient of a large organic dye (rhodamine B isothiocyanate-dextran, referred to as

83 RBID in the following, average molecular weight ~ 70,000 g mol^{-1}) in erythritol-water matrix as a

84 function of water activity (a_w) using the rectangular area fluorescence recovery after photobleaching

85 (rFRAP) technique (Deschout et al., 2010). The diffusion coefficients were then converted to

86 viscosities using the Stokes-Einstein equation, which is expressed as

$$D = k_B T / (6\pi\eta R_H), \tag{1}$$

87 where D is the diffusion coefficient (m^2 s^{-1}); k_B is the Boltzmann constant (1.38×10^{-23} J K^{-1}); T is

88 the temperature (K); η is the viscosity (Pa s) of the matrix and R_H is the hydrodynamic radius (m)

89 of the diffusing species, i.e., RBID. RBID has an R_H that is more than 16 times larger than that of

90 erythritol (Table 1 and Fig. 1). We assume that the viscosity of an erythritol-water particle can be

91 accurately calculated from the diffusion coefficient of RBID and the Stokes-Einstein equation, since

92 the Stokes-Einstein equation accurately predicts diffusion coefficients when the diffusing molecules

93 are large in size relative to the matrix molecules, and when the matrix viscosity is ≲ 10^4 Pa s

94 (Chenyakin et al., 2017; Price et al., 2016), which is the case for erythritol-water particles (Grayson

95 et al., 2017; Song et al., 2016b).

96

97 In addition to determining viscosities from the rFRAP diffusion measurements, we carried out new

98 viscosity measurements for erythritol-water particles at $a_w < 0.1$ using the aerosol optical tweezer

99 technique. The new viscosity results from the rFRAP experiments and the aerosol optical tweezer

100 technique were then used to update our understanding of the viscosity of erythritol-water particles

101 and the effect of adding OH functional groups to a linear C$_4$ carbon backbone on viscosity. The new

102 results also allowed us to perform an intercomparison between three techniques (rFRAP, aerosol

103 optical tweezers and bead-mobility) used for measuring the viscosity of organic-water particles.

104

105

106 **2 Experimental method**

107 **2.1 rFRAP**

108 As mentioned above, the rFRAP technique was used to measure the diffusion coefficient of RBID

109 in erythritol-water matrix as a function of a_w. The rFRAP experiments were similar to those

110 described in Chenyakin et al. (2017). The current rFRAP experiments required thin films (30–50

111 μm thick) with a known a_w, containing erythritol, water, and trace amounts of RBID. Section 2.1.1

112 describes the preparation of the thin films. Section 2.1.2 describes the rFRAP technique and the

113 extraction of diffusion coefficients from the rFRAP data.

Atmospheric
Measurement
Techniques
Discussions

114

2.1.1 Preparation of thin films containing erythritol, water, and trace amounts of RBID with a known a_w

The solubility of erythritol in water at 293 K is ~ 38 weight percent (Haynes, 2015), which corresponds to an $a_w \approx 0.92$, based on Raoult's law and assuming erythritol does not dissociate in water (Koop et al., 2011). In our experiments, all thin films were conditioned at $a_w < 0.92$ and were therefore supersaturated with respect to crystalline erythritol. To prepare these supersaturated thin films, a bulk solution containing 20 weight percent erythritol in water and 0.056 weight percent (0.01 mmol L^{-1}) RBID were prepared gravimetrically. The prepared bulk solution was then filtered using a 0.45 μm Millex®-HV syringe filter unit (Millipore Sigma Ltd., Etobikoe, ON, Canada) to eliminate solid impurities. Next, the solution was nebulized onto a siliconized hydrophobic glass slide (22×22 mm, VWR, Radnor, PA, USA), which had been rinsed with Milli-Q® water (18.2 MΩ cm). This resulted in droplets with radii ranging from 100 to 170 μm on the hydrophobic glass slide. The slide holding the droplets was then transferred into a flow cell in an inflatable glove bag (Glas-Col, Terre Haute, IN, USA) for conditioning at a particular a_w. A handheld hygrometer (OMEGA, Norwalk, CT, USA) with an accuracy of ± 2.5% was used to measure the RH at the flow cell outlet and in the glove bag. The a_w was calculated from the measured RH (i.e. a_w = RH (%) / 100) (Seinfeld and Pandis, 2006). The time used for conditioning droplets ranged from 21.5 to 96 h. See Sect. S1 and Table S1 (Supporting Information) for details. After conditioning the droplets at a particular a_w, thin films were formed by placing a second hydrophobic glass slide on top of the original glass slide supporting the droplets. A pair of aluminum spacers, with a thickness of 30–50 μm, were placed between the two slides to control the thickness of the thin films. A seal was formed between the two slides by lining the perimeter of one slide with high-vacuum grease prior to sandwiching the droplets. Figure S1 (Supporting Information) shows a schematic of the thin films used in the rFRAP experiment. The process of creating the thin films was carried out inside the inflated glove bag, to prevent the sample from being exposed to the uncontrolled room RH. After conditioning the droplets to a known a_w and creating the thin films, the concentration of RBID in the thin films ranged from 0.2 to 0.3 weight percent. At this concentration, the fluorescence intensity of the thin films was proportional to the RBID concentration (Sect. S2 and Fig. S2, Supporting Information).

Even though all thin films were supersaturated with respect to crystalline erythritol, crystallization was not observed, likely because 1) the bulk solution was filtered to remove impurities, and 2) the glass slides were highly hydrophobic, which reduced the possibility of heterogeneous nucleation of organic crystals (Bodsworth et al., 2010; Pant et al., 2004, 2006; Wheeler and Bertram, 2012; Yeung et al., 2009).

2.1.2 rFRAP technique and data extraction

In the rFRAP experiments, a confocal laser scanning microscope was used to photobleach RBID

152 molecules in a small volume of the thin film. After photobleaching, a gradual recovery of

153 fluorescence within the photobleached region occurred due to the diffusion of unbleached

154 fluorescent molecules from outside the bleached region into the bleached region. The diffusion

155 coefficient of the fluorescent dye was determined by monitoring the time-dependent recovery of the

156 fluorescence intensity using the same confocal laser scanning microscope used for photobleaching.

157

158 In this work, a Zeiss LSM510 confocal laser scanning microscope with a 10×/0.30 numerical

159 aperture objective was used. The pinhole was set at 120 μm. Photobleaching was performed using

160 a helium-neon laser with an emission wavelength of 543 nm, at a power of 330 μW. The

161 photobleached area ranged from 3×3 to 6×6 μm^2. The bleach parameters, including the number of

162 iterations and scanning speed of the laser, were adjusted to obtain a reduction in fluorescence

163 intensity of ~ 30% in the bleached region, as recommended by Deschout et al. (2010). After

164 photobleaching, images were taken using the same laser at a power of 4 μW, at time intervals ranging

165 from 2 to 30 s, depending on the speed of recovery of the fluorescence signal, with longer intervals

166 used when the fluorescence recovery was slower. All experiments were performed at room

167 temperature (292–294 K).

168

169 Figure 2 shows an example of a series of images recorded during an rFRAP experiment. All of the

170 images recorded after photobleaching were normalized against an image captured prior to

171 photobleaching, using the ImageJ software. After normalization, the images were downsized from

172 512×512 pixels to 128×128 pixels by averaging pixels to reduce the level of noise (Chenyakin et

173 al., 2017).

174

175 The following is the analytical solution given by Deschout et al. (2010) for the fluorescence intensity

176 at position (x,y) and time t after photobleaching a rectangle area in a thin film:

$$\frac{F(x,y,t)}{F_0(x,y,t)} = 1 - \frac{K_0}{4}\left[\mathrm{erf}\left(\frac{x+\frac{l_x}{2}}{\sqrt{r^2+4Dt}}\right) - \mathrm{erf}\left(\frac{x-\frac{l_x}{2}}{\sqrt{r^2+4Dt}}\right)\right] \times \left[\mathrm{erf}\left(\frac{y+\frac{l_y}{2}}{\sqrt{r^2+4Dt}}\right) - \mathrm{erf}\left(\frac{y-\frac{l_y}{2}}{\sqrt{r^2+4Dt}}\right)\right], \qquad (2)$$

177 where $F(x,y,t)$ is the fluorescence intensity at position (x,y) and time t after photobleaching, $F_0(x,y)$

178 is the fluorescence intensity at position (x,y) prior to photobleaching, l_x and l_y are the lengths of the

179 rectangular photobleached area, K_0 is related to the fraction of molecules photobleached in the

180 bleach region, r is the resolution of the microscope, t is the time after photobleaching, and D is the

181 diffusion coefficient of the fluorescent dye.

182

183 Following the rFRAP experiments, individual images were fit to Eq. (2) using a Matlab script, with

184 K_0 and $r^2 + 4Dt$ left as free parameters. A normalization factor was also included as a free parameter,

185 and it returned a value close to 1, as expected. From Eq. (2), a value of $r^2 + 4Dt$ was obtained for

186 each image taken after photobleaching. Next, $r^2 + 4Dt$ was plotted as a function of time after

187 photobleaching, and a straight line was fit to the plotted data. An example plot of $r^2 + 4Dt$ versus t

Atmospheric
Measurement
Techniques
Discussions

188   and a linear fit to the data are shown in Fig. 3. Diffusion coefficients were determined from the slope

189   of the fitted line. The diffusion coefficient at each a_w reported in Sect. 3 is the average of at least

190   four measurements.

191

192   Cross-sectional views of the fluorescence intensity along the x-axis for different times after

193   photobleaching are shown in Fig. 4. The cross-sections for the measured intensities (blue dots) were

194   generated by averaging the normalized fluorescence intensities (F/F_0) over the width of the

195   photobleached region in the y direction, at each position x. Calculated cross-sections of the

196   fluorescence intensities (red lines) were generated from fits of Eq. (2) to the experimental data. The

197   close agreement between the measured and calculated cross-sections illustrates that Eq. (2)

198   describes our experimental data well.

199

200   Equation (2) was derived by assuming no diffusion in the axial direction (i.e. z-direction). Deschout

201   et al. (2010) have shown that Eq. (2) gives accurate diffusion coefficients when the numerical

202   aperture of the microscope is low (≤ 0.45) and the thickness of the films is small (≤ 120 μm),

203   consistent with the numerical aperture of 0.30 and film thickness of 30–50 μm used in our

204   experiments. Equation (2) also assumes that the only mechanism for recovery in the photobleached

205   region is diffusion. An additional possible mechanism is reversible photobleaching, which has been

206   observed in some fluorescence imaging experiments (Chenyakin et al., 2017; Long et al., 2011;

207   Sinnecker et al., 2005). In a separate set of experiments, we showed that this is not an important

208   mechanism in our experiments (Sect. S3 and Fig. S3, Supporting Information).

209

210   **2.2 Aerosol optical tweezer**

211   The application of the aerosol optical tweezer technique to measure the viscosity of aerosol particles

212   has been discussed in detail in previous publications (Bzdek et al., 2016; Song et al., 2016b) and

213   will only be briefly reviewed here. Two optical traps are formed using a holographic optical tweezers

214   instrument equipped with a laser at 532 nm (Laser Quantum Opus 3W). The holographic

215   arrangement uses a spatial light modulator (Hamamatsu, X10468) to encode phase information into

216   the expanded laser-light wavefront, creating an interference pattern in the trapping plane that

217   resembles two tightly focused beams. Aerosol droplets are captured from a cloud of aerosol

218   generated from a medical nebulizer and introduced into a RH-controlled trapping cell with the RH

219   recorded by a capacitance probe (Honeywell, HIH-4202A). Typical particle diameters are 9–16 μm.

220   Droplet sizes and refractive indices are inferred from the discrete wavelengths commensurate with

221   whispering gallery modes (WGMs) that are observed in the Raman scattering fingerprints recorded

222   from the two droplets. Particle size and refractive index are estimated from comparison with

223   calculated WGM wavelengths using Mie scattering theory and can be determined with an accuracy

224   of $< \pm 2$ nm and $< \pm 0.0005$, respectively (Preston and Reid, 2013).

225

Atmospheric
Measurement
Techniques
Discussions

226   Following a conditioning period of many hours, identified by a steady droplet size over a period of

227   tens of minutes, the particles are coalesced by manipulating the optical trap positions. Once brought

228   into contact, the shape of the composite particle relaxes over a timescale of microseconds to hours,

229   dependent on the viscosity. One of three methods is then chosen to infer particle viscosity from the

230   shape relaxation based on the relaxation timescale:

231

232   (1)   For relaxation timescales of < 1 ms (equivalent to viscosities < 10 Pa s) (Power and

233   Reid, 2014), the time-dependence of the backscattered light intensity can be used to monitor

234   the change in shape using a silicon photodetector (Thorlabs, DET 110) and oscilloscope

235   (LeCroy, HDO 6034-MS). At timescales longer than this, the movement of the trapped

236   particle relative to the laser beam focus (i.e. the relaxation in trapped position) contributes

237   to the change in light scattering signal and becomes convoluted with the change arising

238   from the relaxation in shape. Thus, light scattering measurements cannot be used for

239   viscosities > 10 Pa s (Bzdek et al., 2016).

240   (2)   For longer timescales, the relaxation in shape can be directly viewed from brightfield

241   microscopy over a period spanning from 5 – 10 ms (equivalent to viscosities > 10 Pa s) to

242   as long as 10^3 s (equivalent to viscosities $\sim 10^7$ Pa s) (Bzdek et al., 2016). Images are

243   recorded by a camera (Dalsa Genie HM 640, CMOS) with 5 – 10 ms time resolution. The

244   change in aspect ratio for the relaxing particle is determined and used to determine the

245   relaxation time constant (Song et al., 2016b).

246   (3)   The disappearance followed by the reappearance of WGMs from the Raman

247   spectrum from the coalesced dimer (recorded with 1 s time resolution) can be used to infer

248   the slow disappearance of a spherical cavity on one side of the dimer and reemergence of a

249   single spherical particle at the end of the relaxation process (Power et al., 2013). With a

250   coarse time resolution of 1 s, this method should only be used to infer the viscosity when

251   higher than 10^4 Pa s (Power and Reid, 2014).

252

253   With three analysis methods, viscosity measurement can cover a wide range, from 10^{-3} Pa s to $> 10^9$

254   Pa s. However, it should be noted that there are ranges where two techniques may overlap but with

255   varying accuracy (e.g. imaging and Raman for viscosities $10^4 – 10^5$ Pa s with relaxation times of 1

256   – 10 s).

257

258

259   **3   Results and Discussion**

260   **3.1 Diffusion coefficients in and viscosities of erythritol-water particles as functions of a_w**

261   **measured by the rFRAP technique**

262   Shown in Fig. 5(a) and listed in Table S2 (Supporting Information) are the measured diffusion

263   coefficients of RBID in erythritol-water matrices as a function of a_w. The diffusion coefficient

264 decreased by $2 - 3$ orders of magnitude as a_w decreased from approximately 0.5 to 0. This decrease

265 in the diffusion coefficients with a decrease in a_w is due to the plasticizing effect of water (Koop et

266 al., 2011; Power et al., 2013).

267

268 The Stokes-Einstein equation and measured diffusion coefficients were used to calculate the

269 viscosity of erythritol-water particles. It has been found that the Stokes-Einstein equation

270 significantly underestimates the diffusion coefficients of small molecules such as water and ozone

271 within a matrix containing larger molecules (Bastelberger et al., 2017; Li et al., 2015; Marshall et

272 al., 2016; Price et al., 2014; Shiraiwa et al., 2011). On the other hand, as discussed in Sect. 1, the

273 Stokes-Einstein equation gives accurate diffusion coefficients when the diffusing species is similar

274 in size or larger than the matrix molecules and when the viscosity of the matrix is comparable to or

275 lower than 10^4 Pa s (Chenyakin et al., 2017; Price et al., 2016). Hence, in this study, we assume that

276 the viscosity of erythritol-water particles can be accurately calculated using the measured RBID

277 diffusion coefficient and the Stokes-Einstein equation, because RBID is much larger than the matrix

278 molecules (Table 1) and the highest reported viscosity of erythritol in the literature is on the order

279 of 10^4 Pa s (Grayson et al., 2017; Song et al., 2016b).

280

281 Figure 5(b) and Table S2 show the viscosity of erythritol-water particles (calculated using diffusion

282 coefficients from Fig. 5(a) and the Stokes-Einstein equation) as a function of a_w. As a_w decreased

283 from approximately 0.5 to 0, the viscosity increased from approximately 1×10^{-1} to 5×10^1 Pa s.

284 The symbols in Fig. 5 are color-coded by the time allowed to condition the samples to a particular

285 a_w value before measuring the diffusion coefficient. The color scale in the top left corner applies to

286 both panels (a) and (b). No clear trend is observed between the conditioning time and diffusion

287 coefficient or particle viscosity.

288

289 To further investigate the effect of the time used to condition the samples to a particular a_w value,

290 in Fig. 6, the measured RBID diffusion coefficients in erythritol-water matrices are plotted as a

291 function of conditioning time at $a_w \leq 0.105$. The data shown in Fig. 6 were taken from the data

292 shown in Fig. 5(a). Included as a secondary x-axis is the sample conditioning time in multiples of

293 τ_w, where τ_w is the characteristic time for water diffusion within the sample droplets used in the

294 conditioning experiments (see Sect. S1 for details, Supporting Information). Consistent with Fig.

295 5(a), Fig. 6 illustrates that there is no clear trend between diffusion coefficient and the time allowed

296 for conditioning the samples prior to the diffusion measurements. Figure 6 also suggests that a

297 sample conditioning time of ≥ 21.5 hours, or ≥ 6.5 τ_w was sufficient to reach near equilibrium

298 between the RH used for conditioning and the a_w in particles.

299

300 **3.2 Viscosity of erythritol-water particles as a function of a_w measured by the aerosol optical**

301 **tweezer technique**

302   Erythritol viscosity measurements using the aerosol optical tweezer technique are shown in Fig. 7.

303   The viscosity of pure water at 293 K (Korson et al., 1969) is also included for comparison. The red

304   circles represent the new aerosol optical tweezer measurements obtained in this work (also listed in

305   Table S3, Supporting Information), based solely on brightfield images. The gray circles represent

306   the viscosities reported in Song et al. (2016b). The new averaged viscosities reported here based on

307   the aerosol optical tweezer technique are lower than those reported by Song et al. (2016b) at $a_w <$

308   0.1, although the error bars (representing two standard deviations) overlap.

309

310   In the previous aerosol optical tweezer measurements at $a_w < 0.1$ (Song et al., 2016b), the timescale

311   for relaxation to a sphere was estimated from two methods: the change in coalesced particle shape

312   as recorded by the brightfield images and the reappearance of WGMs in the Raman spectrum. Upon

313   re-evaluation of the data previously obtained at $a_w < 0.1$ (Song et al., 2016b) and comparison with

314   the new measurements, it was determined that erythritol viscosity measurements under dry

315   conditions using the Raman spectral measurements were compromised by the limited time

316   resolution (1 s, equivalent to ~ 10^4 Pa s) and higher than those estimated from brightfield imaging,

317   yielding an overestimate of the viscosity. Since the new aerosol optical tweezer measurements in

318   this work are based solely on the brightfield images, they are more accurate than the previous results

319   at $a_w < 0.1$ as a consequence of the higher time resolution of the brightfield imaging measurement

320   compared to the Raman spectroscopy measurement. The viscosity at $a_w = 0.22$ reported by Song et

321   al. (2016b) was based on brightfield images alone and those at $a_w \geq 0.43$ were based on back-

322   scattered light intensity (where viscosities were < 10 Pa s, see Sect. 2.2).

323

324   **3.3 Update on the viscosity of erythritol-water particles as a function of a_w and an**

325   **intercomparison of techniques for measuring the viscosity of particles**

326   In Fig. 8, we have summarized the previous and current measurements of the viscosity of erythritol-

327   water particles as a function of a_w. The black triangles represent measurements by Grayson et al.

328   (2017) using the bead-mobility technique. The blue squares represent the rFRAP results from this

329   work, where experimental data at similar a_w have been binned together so as not to give extra weight

330   to the rFRAP data. The red circles indicate aerosol optical tweezer measurements from Song et al.

331   (2016b) (open circles) and this study (solid circles). The previous measurements at $a_w \leq 0.1$ by Song

332   et al. (2016b) were excluded from Fig. 8, because the new aerosol optical tweezer measurements

333   reported in this study at $a_w \leq 0.1$ are thought to be more accurate. Considering the uncertainties in

334   the measurements, the results from the three techniques (bead-mobility, rFRAP and aerosol optical

335   tweezer) are in reasonable agreement.

336

337   To determine the viscosity of pure erythritol under dry conditions ($a_w = 0$), a straight line was fit to

338   the data in Fig. 8 (shown as the red line) and then extrapolated to $a_w = 0$. The intercept on the y-axis

339   was 2.393 ± 0.246 (two standard deviations), corresponding to a viscosity of pure erythritol of

Atmospheric
Measurement
Techniques
Discussions

Open Access

EGU

340   247^{+188}_{-107} Pa s.

341

342   **3.4 Effect of the addition of OH functional groups to a linear C$_4$ carbon backbone**

343   Grayson et al. (2017) previously estimated the effect of adding OH functional groups on the

344   viscosity of a linear C$_4$ compound. Here we repeat this analysis (Fig. 9) based on the updated

345   viscosity of pure erythritol (247^{+188}_{-107} Pa s) determined above. For those compounds with the same

346   number but different positions of OH functional groups, the average of their viscosities was taken

347   from the literature (Grayson et al., 2017; Rothfuss and Petters, 2017; Song et al., 2016b). Table S4

348   (Supporting Information) lists the values and sources of literature data used. The data in Fig. 9 were

349   fit to a linear equation, resulting in a slope of 1.437 ± 0.090 (two standard deviations), which

350   indicates that the viscosity of a linear C$_4$ molecule increases on average by a factor of 27^{+6}_{-5} per

351   addition of an OH functional group.

352

353   The viscosity increase from the addition of OH functional groups to a carbon backbone may depend

354   on the level of prior functionalization. To investigate this aspect further, we calculated the sensitivity

355   parameter (S_η) for a linear C$_4$ carbon backbone using the viscosity data presented in Fig. 9 and the

356   following equation (Rothfuss and Petters, 2017):

$$S_\eta = \Delta\log_{10}(\eta\,/\,\text{Pa s})\,/\,\Delta N, \tag{3}$$

357   where $\Delta\log_{10}(\eta\,/\,\text{Pa s})$ is the change in viscosity on a $\log_{10}$ scale, and ΔN is the change in the number

358   of OH functional groups. S_η was estimated based on the addition of one OH functional group (ΔN

359   = 1), starting from n-butane. The relationship between S_η and N is shown in Fig. 10 for a linear C$_4$

360   carbon backbone. S_η is between 0.7 and 1.9 for $N = 1 - 3$. On the other hand, S_η is between 1.7 and

361   2.7 for $N = 4$, suggesting S_η increases with the addition of the fourth OH functional group to the

362   linear C$_4$ carbon backbone. However, additional studies are needed in order to reduce the

363   uncertainties of the measurements and make stronger conclusions.

364

365

366   **4   Summary and Conclusion**

367   In this work, viscosities of erythritol-water particles as a function of a_w at 292 – 295 K were

368   measured using the rFRAP and aerosol optical tweezer techniques. In the rFRAP measurements, a

369   trace amount of RBID (0.2 – 0.3 weight percent) was added to the erythritol-water matrix and

370   viscosities of erythritol-water particles were estimated based on the measured diffusion coefficients

371   of RBID and the Stokes-Einstein equation. In the new measurements using the aerosol optical

372   tweezer technique, viscosity was measured at $a_w < 0.1$ based solely on brightfield imaging (Song et

373   al., 2016b).

374

375   In general, considering the uncertainties in the measurements, viscosities measured using the bead-

376   mobility (Grayson et al., 2017), rFRAP and aerosol optical tweezer techniques are in reasonable

377   agreement. A linear fit was performed for the experimentally determined viscosities of erythritol-

378   water particles against a_w and extrapolated to $a_w = 0$. Based on the extrapolation, the viscosity of

379   pure erythritol at 292 – 295 K is estimated at 247^{+188}_{-107} Pa s (two standard deviations). Based on

380   these results, the addition of an OH functional group to a linear C_4 carbon backbone increased the

381   viscosity by a factor of 27^{+6}_{-5} (two standard deviations), on average. In comparison, Grayson et al.

382   (2017) reported a factor of 41^{+27}_{-16} based on previous measurements.

383

384   The sensitivity parameter was calculated to determine the dependency of viscosity on the degree of

385   prior functionalization for a linear C_4 carbon backbone. Based on the sensitivity parameter analysis,

386   the increase in viscosity due to the addition of one OH functional group to a linear C_4 carbon

387   backbone is not a strong function of the number of OH groups already present in the molecule, up

388   to the addition of three OH functional groups. On the other hand, the degree of increase in viscosity

389   is likely larger when the linear C_4 carbon backbone already contains three OH groups. These results

390   should help improve the understanding of the viscosity of SOA particles in the atmosphere.

391

392   **Data availability.**

393   Data for this paper are available in the Supporting Information.

394

395   **Competing interests.**

396   The authors declare that they have no conflict of interest.

397

398   **Acknowledgments.**

406

Atmospheric
Measurement
Techniques
Discussions

407 **References**

408 Abramson, E., Imre, D., Beránek, J., Wilson, J. and Zelenyuk, A.: Experimental determination of

409 chemical diffusion within secondary organic aerosol particles, Phys. Chem. Chem. Phys., 15(8), 2983–

410 2991, doi:10.1039/c2cp44013j, 2013.

411 Adler, G., Koop, T., Haspel, C., Taraniuk, I., Moise, T., Koren, I., Heiblum, R. H. and Rudich, Y.:

412 Formation of highly porous aerosol particles by atmospheric freeze-drying in ice clouds, Proc. Natl.

413 Acad. Sci., 110(51), 20414–20419, doi:10.1073/pnas.1317209110, 2013.

414 Bastelberger, S., Krieger, U. K., Luo, B. and Peter, T.: Diffusivity measurements of volatile organics in

415 levitated viscous aerosol particles, Atmos. Chem. Phys., 17(13), 8453–8471, doi:10.5194/acp-17-8453-

416 2017, 2017.

417 Bateman, A. P., Bertram, A. K. and Martin, S. T.: Hygroscopic Influence on the Semisolid-to-Liquid

418 Transition of Secondary Organic Materials, J. Phys. Chem. A, 119(19), 4386–4395,

419 doi:10.1021/jp508521c, 2015.

420 Bateman, A. P., Gong, Z., Liu, P., Sato, B., Cirino, G., Zhang, Y., Artaxo, P., Bertram, A. K., Manzi,

421 A. O., Rizzo, L. V, Souza, R. A. F., Zaveri, R. A. and Martin, S. T.: Sub-micrometre particulate matter

422 is primarily in liquid form over Amazon rainforest, Nat. Geosci., 9(1), 34–37, doi:10.1038/ngeo2599,

423 2016.

424 Bateman, A. P., Gong, Z., Harder, T. H., de Sá, S. S., Wang, B., Castillo, P., China, S., Liu, Y.,

425 O'Brien, R. E., Palm, B. B., Shiu, H.-W., Cirino, G. G., Thalman, R., Adachi, K., Alexander, M. L.,

426 Artaxo, P., Bertram, A. K., Buseck, P. R., Gilles, M. K., Jimenez, J. L., Laskin, A., Manzi, A. O.,

427 Sedlacek, A., Souza, R. A. F., Wang, J., Zaveri, R. and Martin, S. T.: Anthropogenic influences on the

428 physical state of submicron particulate matter over a tropical forest, Atmos. Chem. Phys., 17(3), 1759–

429 1773, doi:10.5194/acp-17-1759-2017, 2017.

430 Baustian, K. J., Wise, M. E., Jensen, E. J., Schill, G. P., Freedman, M. A. and Tolbert, M. A.: State

431 transformations and ice nucleation in amorphous (semi-)solid organic aerosol, Atmos. Chem. Phys.,

432 13(11), 5615–5628, doi:10.5194/acp-13-5615-2013, 2013.

433 Berkemeier, T., Steimer, S. S., Krieger, U. K., Peter, T., Poschl, U., Ammann, M. and Shiraiwa, M.:

434 Ozone uptake on glassy, semi-solid and liquid organic matter and the role of reactive oxygen

435 intermediates in atmospheric aerosol chemistry, Phys. Chem. Chem. Phys., 18(18), 12662–12674,

436 doi:10.1039/C6CP00634E, 2016.

Atmospheric
Measurement
Techniques
Discussions

437   Bodsworth, A., Zobrist, B. and Bertram, A. K.: Inhibition of efflorescence in mixed organic-inorganic

438   particles at temperatures less than 250 K, Phys. Chem. Chem. Phys., 12(38), 12259–12266,

439   doi:10.1039/C0CP00572J, 2010.

440   Bones, D. L., Reid, J. P., Lienhard, D. M. and Krieger, U. K.: Comparing the mechanism of water

441   condensation and evaporation in glassy aerosol, Proc. Natl. Acad. Sci., 109(29), 11613–11618,

442   doi:10.1073/pnas.1200691109, 2012.

443   Bzdek, B. R., Collard, L., Sprittles, J. E., Hudson, A. J. and Reid, J. P.: Dynamic measurements and

444   simulations of airborne picolitre-droplet coalescence in holographic optical tweezers, J. Chem. Phys.,

445   145(5), 54502, doi:10.1063/1.4959901, 2016.

446   Cappa, C. D. and Wilson, K. R.: Evolution of organic aerosol mass spectra upon heating: implications

447   for OA phase and partitioning behavior, Atmos. Chem. Phys., 11(5), 1895–1911, doi:10.5194/acp-11-

448   1895-2011, 2011.

449   Chenyakin, Y., Ullmann, D. A., Evoy, E., Renbaum-Wolff, L., Kamal, S. and Bertram, A. K.:

450   Diffusion coefficients of organic molecules in sucrose-water solutions and comparison with Stokes-

451   Einstein predictions, Atmos. Chem. Phys., 17(3), 2423–2435, doi:10.5194/acp-17-2423-2017, 2017.

452   Chu, Y. and Chan, C. K.: Reactive Uptake of Dimethylamine by Ammonium Sulfate and Ammonium

453   Sulfate–Sucrose Mixed Particles, J. Phys. Chem. A, 121(1), 206–215, doi:10.1021/acs.jpca.6b10692,

454   2017a.

455   Chu, Y. and Chan, C. K.: Role of oleic acid coating in the heterogeneous uptake of dimethylamine by

456   ammonium sulfate particles, Aerosol Sci. Technol., 51(8), 988–997,

457   doi:10.1080/02786826.2017.1323072, 2017b.

458   Claeys, M.: Formation of Secondary Organic Aerosols Through Photooxidation of Isoprene, Science

459   (80-.)., 303(5661), 1173–1176, doi:10.1126/science.1092805, 2004.

460   Deschout, H., Hagman, J., Fransson, S., Jonasson, J., Rudemo, M., Lorén, N. and Braeckmans, K.:

461   Straightforward FRAP for quantitative diffusion measurements with a laser scanning microscope, Opt.

462   Express, 18(22), 22886–22905, doi:10.1364/OE.18.022886, 2010.

463   Edney, E. O., Kleindienst, T. E., Jaoui, M., Lewandowski, M., Offenberg, J. H., Wang, W. and Claeys,

464   M.: Formation of 2-methyl tetrols and 2-methylglyceric acid in secondary organic aerosol from

465   laboratory irradiated isoprene/NO_X/SO_2/air mixtures and their detection in ambient $PM_{2.5}$ samples

466   collected in the eastern United States, Atmos. Environ., 39(29), 5281–5289,

Atmospheric
Measurement
Techniques
Discussions

Open Access
EGU

467   doi:10.1016/j.atmosenv.2005.05.031, 2005.

468   Floury, J., Mourdi, I. El, Silva, J. V. C., Lortal, S., Thierry, A. and Jeanson, S.: Diffusion of solutes

469   inside bacterial colonies immobilized in model cheese depends on their physicochemical properties: a

470   time-lapse microscopy study, Front. Microbiol., 6, 366, doi:10.3389/fmicb.2015.00366, 2015.

471   Gatzsche, K., Iinuma, Y., Tilgner, A., Mutzel, A., Berndt, T. and Wolke, R.: Kinetic modeling studies

472   of SOA formation from α-pinene ozonolysis, Atmos. Chem. Phys., 17(21), 13187–13211,

473   doi:10.5194/acp-17-13187-2017, 2017.

474   Grayson, J. W., Zhang, Y., Mutzel, A., Renbaum-Wolff, L., Böge, O., Kamal, S., Herrmann, H.,

475   Martin, S. T. and Bertram, A. K.: Effect of varying experimental conditions on the viscosity of α-

476   pinene derived secondary organic material, Atmos. Chem. Phys., 16(10), 6027–6040, doi:10.5194/acp-

477   16-6027-2016, 2016.

478   Grayson, J. W., Evoy, E., Song, M., Chu, Y., Maclean, A., Nguyen, A., Upshur, M. A., Ebrahimi, M.,

479   Chan, C. K., Geiger, F. M., Thomson, R. J. and Bertram, A. K.: The effect of hydroxyl functional

480   groups and molar mass on the viscosity of non-crystalline organic and organic–water particles, Atmos.

481   Chem. Phys., 17(13), 8509–8524, doi:10.5194/acp-17-8509-2017, 2017.

482   Hallquist, M., Wenger, J. C., Baltensperger, U., Rudich, Y., Simpson, D., Claeys, M., Dommen, J.,

483   Donahue, N. M., George, C., Goldstein, A. H., Hamilton, J. F., Herrmann, H., Hoffmann, T., Iinuma,

484   Y., Jang, M., Jenkin, M. E., Jimenez, J. L., Kiendler-Scharr, A., Maenhaut, W., McFiggans, G., Mentel,

485   T. F., Monod, A., Prévôt, A. S. H., Seinfeld, J. H., Surratt, J. D., Szmigielski, R. and Wildt, J.: The

486   formation, properties and impact of secondary organic aerosol: current and emerging issues, Atmos.

487   Chem. Phys., 9(14), 5155–5236, doi:10.5194/acp-9-5155-2009, 2009.

488   Haynes, W. M., Ed.: CRC Handbook of Chemistry and Physics, 96th ed., CRC Press., 2015.

489   Hinks, M. L., Brady, M. V, Lignell, H., Song, M., Grayson, J. W., Bertram, A. K., Lin, P., Laskin, A.,

490   Laskin, J. and Nizkorodov, S. A.: Effect of viscosity on photodegradation rates in complex secondary

491   organic aerosol materials, Phys. Chem. Chem. Phys., 18(13), 8785–8793, doi:10.1039/C5CP05226B,

492   2016.

493   Hosny, N. A., Fitzgerald, C., Vysniauskas, A., Athanasiadis, A., Berkemeier, T., Uygur, N., Poschl, U.,

494   Shiraiwa, M., Kalberer, M., Pope, F. D. and Kuimova, M. K.: Direct imaging of changes in aerosol

495   particle viscosity upon hydration and chemical aging, Chem. Sci., 7(2), 1357–1367,

496   doi:10.1039/C5SC02959G, 2016.

Atmospheric
Measurement
Techniques
Discussions

497   Houle, F. A., Hinsberg, W. D. and Wilson, K. R.: Oxidation of a model alkane aerosol by OH radical:

498   the emergent nature of reactive uptake, Phys. Chem. Chem. Phys., 17(6), 4412–4423,

499   doi:10.1039/C4CP05093B, 2015.

500   Ignatius, K., Kristensen, T. B., Järvinen, E., Nichman, L., Fuchs, C., Gordon, H., Herenz, P., Hoyle, C.

501   R., Duplissy, J., Garimella, S., Dias, A., Frege, C., Höppel, N., Tröstl, J., Wagner, R., Yan, C.,

502   Amorim, A., Baltensperger, U., Curtius, J., Donahue, N. M., Gallagher, M. W., Kirkby, J., Kulmala,

503   M., Möhler, O., Saathoff, H., Schnaiter, M., Tomé, A., Virtanen, A., Worsnop, D. and Stratmann, F.:

504   Heterogeneous ice nucleation of viscous secondary organic aerosol produced from ozonolysis of α-

505   pinene, Atmos. Chem. Phys., 16(10), 6495–6509, doi:10.5194/acp-16-6495-2016, 2016.

506   Jimenez, J. L., Canagaratna, M. R., Donahue, N. M., Prevot, A. S. H., Zhang, Q., Kroll, J. H., DeCarlo,

507   P. F., Allan, J. D., Coe, H., Ng, N. L., Aiken, A. C., Docherty, K. S., Ulbrich, I. M., Grieshop, A. P.,

508   Robinson, A. L., Duplissy, J., Smith, J. D., Wilson, K. R., Lanz, V. A., Hueglin, C., Sun, Y. L., Tian,

509   J., Laaksonen, A., Raatikainen, T., Rautiainen, J., Vaattovaara, P., Ehn, M., Kulmala, M., Tomlinson, J.

510   M., Collins, D. R., Cubison, M. J., Dunlea, J., Huffman, J. A., Onasch, T. B., Alfarra, M. R., Williams,

511   P. I., Bower, K., Kondo, Y., Schneider, J., Drewnick, F., Borrmann, S., Weimer, S., Demerjian, K.,

512   Salcedo, D., Cottrell, L., Griffin, R., Takami, A., Miyoshi, T., Hatakeyama, S., Shimono, A., Sun, J. Y.,

513   Zhang, Y. M., Dzepina, K., Kimmel, J. R., Sueper, D., Jayne, J. T., Herndon, S. C., Trimborn, A. M.,

514   Williams, L. R., Wood, E. C., Middlebrook, A. M., Kolb, C. E., Baltensperger, U. and Worsnop, D. R.:

515   Evolution of Organic Aerosols in the Atmosphere, Science (80-.)., 326(5959), 1525–1529,

516   doi:10.1126/science.1180353, 2009.

517   Kanakidou, M., Seinfeld, J. H., Pandis, S. N., Barnes, I., Dentener, F. J., Facchini, M. C., Van

518   Dingenen, R., Ervens, B., Nenes, A., Nielsen, C. J., Swietlicki, E., Putaud, J. P., Balkanski, Y., Fuzzi,

519   S., Horth, J., Moortgat, G. K., Winterhalter, R., Myhre, C. E. L., Tsigaridis, K., Vignati, E., Stephanou,

520   E. G. and Wilson, J.: Organic aerosol and global climate modelling: a review, Atmos. Chem. Phys., 5,

521   1053–1123, doi:10.5194/acp-5-1053-2005, 2005.

522   Kiyosawa, K.: Volumetric properties of polyols (ethylene glycol, glycerol, meso-erythritol, xylitol and

523   mannitol) in relation to their membrane permeability: Group additivity and estimation of the maximum

524   radius of their molecules, Biochim. Biophys. Acta - Biomembr., 1064(2), 251–255, doi:10.1016/0005-

525   2736(91)90309-V, 1991.

526   Koop, T., Bookhold, J., Shiraiwa, M. and Pöschl, U.: Glass transition and phase state of organic

Atmospheric
Measurement
Techniques
Discussions

527   compounds: dependency on molecular properties and implications for secondary organic aerosols in

528   the atmosphere, Phys. Chem. Chem. Phys., 13(43), 19238–19255, doi:10.1039/c1cp22617g, 2011.

529   Korson, L., Drost-Hansen, W. and Millero, F. J.: Viscosity of water at various temperatures, J. Phys.

530   Chem., 73(1), 34–39, doi:10.1021/j100721a006, 1969.

531   Kuwata, M. and Martin, S. T.: Phase of atmospheric secondary organic material affects its reactivity,

532   Proc. Natl. Acad. Sci., 109(43), 17354–17359, doi:10.1073/pnas.1209071109, 2012.

533   Ladino, L. A., Zhou, S., Yakobi-Hancock, J. D., Aljawhary, D. and Abbatt, J. P. D.: Factors controlling

534   the ice nucleating abilities of α-pinene SOA particles, J. Geophys. Res. Atmos., 119(14), 9041–9051,

535   doi:10.1002/2014JD021578, 2014.

536   Li, Y. J., Liu, P., Gong, Z., Wang, Y., Bateman, A. P., Bergoend, C., Bertram, A. K. and Martin, S. T.:

537   Chemical Reactivity and Liquid/Nonliquid States of Secondary Organic Material, Environ. Sci.

538   Technol., 49(22), 13264–13274, doi:10.1021/acs.est.5b03392, 2015.

539   Lignell, H., Hinks, M. L. and Nizkorodov, S. A.: Exploring matrix effects on photochemistry of

540   organic aerosols, Proc. Natl. Acad. Sci., 111(38), 13780–13785, doi:10.1073/pnas.1322106111, 2014.

541   Liu, P., Li, Y. J., Wang, Y., Bateman, A. P., Zhang, Y., Gong, Z., Bertram, A. K. and Martin, S. T.:

542   Highly Viscous States Affect the Browning of Atmospheric Organic Particulate Matter, ACS Cent.

543   Sci., doi:10.1021/acscentsci.7b00452, 2018.

544   Long, D., Lin, H. and Scheblykin, I. G.: Carbon nanotubes as photoprotectors of organic dyes:

545   reversible photoreaction instead of permanent photo-oxidation, Phys. Chem. Chem. Phys., 13(13),

546   5771–5777, doi:10.1039/C0CP02764B, 2011.

547   Lu, J. W., Rickards, A. M. J., Walker, J. S., Knox, K. J., Miles, R. E. H., Reid, J. P. and Signorell, R.:

548   Timescales of water transport in viscous aerosol: measurements on sub-micron particles and

549   dependence on conditioning history, Phys. Chem. Chem. Phys., 16(21), 9819–9830,

550   doi:10.1039/C3CP54233E, 2014.

551   Maclean, A. M., Butenhoff, C. L., Grayson, J. W., Barsanti, K., Jimenez, J. L. and Bertram, A. K.:

552   Mixing times of organic molecules within secondary organic aerosol particles: a global planetary

553   boundary layer perspective, Atmos. Chem. Phys., 17(21), 13037–13048, doi:10.5194/acp-17-13037-

554   2017, 2017.

555   Marshall, F. H., Miles, R. E. H., Song, Y.-C., Ohm, P. B., Power, R. M., Reid, J. P. and Dutcher, C. S.:

556   Diffusion and reactivity in ultraviscous aerosol and the correlation with particle viscosity, Chem. Sci.,

557   7(2), 1298–1308, doi:10.1039/C5SC03223G, 2016.

558   Mikhailov, E., Vlasenko, S., Martin, S. T., Koop, T. and Pöschl, U.: Amorphous and crystalline aerosol

559   particles interacting with water vapor: conceptual framework and experimental evidence for

560   restructuring, phase transitions and kinetic limitations, Atmos. Chem. Phys., 9(24), 9491–9522,

561   doi:10.5194/acp-9-9491-2009, 2009.

562   Murray, B. J. and Bertram, A. K.: Inhibition of solute crystallisation in aqueous H^+-NH_4^+-SO_4^{2-}-H_2O

563   droplets, Phys. Chem. Chem. Phys., 10(22), 3287–3301, doi:10.1039/B802216J, 2008.

564   O'Brien, R. E., Neu, A., Epstein, S. A., MacMillan, A. C., Wang, B., Kelly, S. T., Nizkorodov, S. A.,

565   Laskin, A., Moffet, R. C. and Gilles, M. K.: Physical properties of ambient and laboratory-generated

566   secondary organic aerosol, Geophys. Res. Lett., 41(12), 4347–4353, doi:10.1002/2014GL060219,

567   2014.

568   Paës, G., Habrant, A., Ossemond, J. and Chabbert, B.: Exploring accessibility of pretreated poplar cell

569   walls by measuring dynamics of fluorescent probes, Biotechnol. Biofuels, 10(1), 15,

570   doi:10.1186/s13068-017-0704-5, 2017.

571   Pajunoja, A., Malila, J., Hao, L., Joutsensaari, J., Lehtinen, K. E. J. and Virtanen, A.: Estimating the

572   Viscosity Range of SOA Particles Based on Their Coalescence Time, Aerosol Sci. Technol., 48(2), i–

573   iv, doi:10.1080/02786826.2013.870325, 2014.

574   Pajunoja, A., Hu, W., Leong, Y. J., Taylor, N. F., Miettinen, P., Palm, B. B., Mikkonen, S., Collins, D.

575   R., Jimenez, J. L. and Virtanen, A.: Phase state of ambient aerosol linked with water uptake and

576   chemical aging in the southeastern US, Atmos. Chem. Phys., 16(17), 11163–11176, doi:10.5194/acp-

577   16-11163-2016, 2016.

578   Pant, A., Fok, A., Parsons, M. T., Mak, J. and Bertram, A. K.: Deliquescence and crystallization of

579   ammonium sulfate-glutaric acid and sodium chloride-glutaric acid particles, Geophys. Res. Lett.,

580   31(12), L12111, doi:10.1029/2004GL020025, 2004.

581   Pant, A., Parsons, M. T. and Bertram, A. K.: Crystallization of Aqueous Ammonium Sulfate Particles

582   Internally Mixed with Soot and Kaolinite: Crystallization Relative Humidities and Nucleation Rates, J.

583   Phys. Chem. A, 110(28), 8701–8709, doi:10.1021/jp060985s, 2006.

584   Perraud, V., Bruns, E. A., Ezell, M. J., Johnson, S. N., Yu, Y., Alexander, M. L., Zelenyuk, A., Imre,

585   D., Chang, W. L., Dabdub, D., Pankow, J. F. and Finlayson-Pitts, B. J.: Nonequilibrium atmospheric

586   secondary organic aerosol formation and growth, Proc. Natl. Acad. Sci., 109(8), 2836–2841,

Atmospheric
Measurement
Techniques
Discussions

587   doi:10.1073/pnas.1119909109, 2012.

588   Power, R. M. and Reid, J. P.: Probing the micro-rheological properties of aerosol particles using optical

589   tweezers, Reports Prog. Phys., 77(7), 74601, doi:10.1088/0034-4885/77/7/074601, 2014.

590   Power, R. M., Simpson, S. H., Reid, J. P. and Hudson, A. J.: The transition from liquid to solid-like

591   behaviour in ultrahigh viscosity aerosol particles, Chem. Sci., 4(6), 2597–2604,

592   doi:10.1039/c3sc50682g, 2013.

593   Preston, T. C. and Reid, J. P.: Accurate and efficient determination of the radius, refractive index, and

594   dispersion of weakly absorbing spherical particle using whispering gallery modes, J. Opt. Soc. Am. B,

595   30(8), 2113–2122, doi:10.1364/JOSAB.30.002113, 2013.

596   Price, H. C., Murray, B. J., Mattsson, J., O'Sullivan, D., Wilson, T. W., Baustian, K. J. and Benning, L.

597   G.: Quantifying water diffusion in high-viscosity and glassy aqueous solutions using a Raman isotope

598   tracer method, Atmos. Chem. Phys., 14(8), 3817–3830, doi:10.5194/acp-14-3817-2014, 2014.

599   Price, H. C., Mattsson, J. and Murray, B. J.: Sucrose diffusion in aqueous solution, Phys. Chem. Chem.

600   Phys., 18(28), 19207–19216, doi:10.1039/C6CP03238A, 2016.

601   Reid, J. P., Bertram, A. K., Topping, D. O., Laskin, A., Martin, S. T., Petters, M. D., Pope, F. D. and

602   Rovelli, G.: The viscosity of atmospherically relevant organic particles, Nat. Commun., 9(1), 956,

603   doi:10.1038/s41467-018-03027-z, 2018.

604   Renbaum-Wolff, L., Grayson, J. W., Bateman, A. P., Kuwata, M., Sellier, M., Murray, B. J., Shilling,

605   J. E., Martin, S. T. and Bertram, A. K.: Viscosity of α-pinene secondary organic material and

606   implications for particle growth and reactivity, Proc. Natl. Acad. Sci., 110(20), 8014–8019,

607   doi:10.1073/pnas.1219548110, 2013.

608   Robinson, C. B., Schill, G. P. and Tolbert, M. A.: Optical growth of highly viscous organic/sulfate

609   particles, J. Atmos. Chem., 71(2), 145–156, doi:10.1007/s10874-014-9287-8, 2014.

610   Rothfuss, N. E. and Petters, M. D.: Influence of Functional Groups on the Viscosity of Organic

611   Aerosol, Environ. Sci. Technol., 51(1), 271–279, doi:10.1021/acs.est.6b04478, 2017.

612   Saleh, R., Donahue, N. M. and Robinson, A. L.: Time Scales for Gas-Particle Partitioning Equilibration

613   of Secondary Organic Aerosol Formed from Alpha-Pinene Ozonolysis, Environ. Sci. Technol., 47(11),

614   5588–5594, doi:10.1021/es400078d, 2013.

615   Schill, G. P., De Haan, D. O. and Tolbert, M. A.: Heterogeneous Ice Nucleation on Simulated

616   Secondary Organic Aerosol, Environ. Sci. Technol., 48(3), 1675–1682, doi:10.1021/es4046428, 2014.

Atmospheric
Measurement
Techniques
Discussions

617   Schultz, S. G. and Solomon, A. K.: Determination of the Effective Hydrodynamic Radii of Small

618   Molecules by Viscometry, J. Gen. Physiol., 44(6), 1189–1199, doi:10.1085/jgp.44.6.1189, 1961.

619   Seinfeld, J. H. and Pandis, S. N.: Atmospheric Chemistry and Physics: From Air Pollution to Climate

620   Change, 2nd Edition, Wiley., 2006.

621   Shiraiwa, M. and Seinfeld, J. H.: Equilibration timescale of atmospheric secondary organic aerosol

622   partitioning, Geophys. Res. Lett., 39(24), L24801, doi:10.1029/2012GL054008, 2012.

623   Shiraiwa, M., Ammann, M., Koop, T. and Poschl, U.: Gas uptake and chemical aging of semisolid

624   organic aerosol particles, Proc. Natl. Acad. Sci., 108(27), 11003–11008,

625   doi:10.1073/pnas.1103045108, 2011.

626   Shiraiwa, M., Li, Y., Tsimpidi, A. P., Karydis, V. A., Berkemeier, T., Pandis, S. N., Lelieveld, J.,

627   Koop, T. and Pöschl, U.: Global distribution of particle phase state in atmospheric secondary organic

628   aerosols, Nat. Commun., 8, 15002, doi:10.1038/ncomms15002, 2017.

629   Shrivastava, M., Lou, S., Zelenyuk, A., Easter, R. C., Corley, R. A., Thrall, B. D., Rasch, P. J., Fast, J.

630   D., Massey Simonich, S. L., Shen, H. and Tao, S.: Global long-range transport and lung cancer risk

631   from polycyclic aromatic hydrocarbons shielded by coatings of organic aerosol, Proc. Natl. Acad. Sci.,

632   114(6), 1246–1251, doi:10.1073/pnas.1618475114, 2017.

633   Sinnecker, D., Voigt, P., Hellwig, N. and Schaefer, M.: Reversible Photobleaching of Enhanced Green

634   Fluorescent Proteins, Biochemistry, 44(18), 7085–7094, doi:10.1021/bi047881x, 2005.

635   Song, M., Liu, P. F., Hanna, S. J., Li, Y. J., Martin, S. T. and Bertram, A. K.: Relative humidity-

636   dependent viscosities of isoprene-derived secondary organic material and atmospheric implications for

637   isoprene-dominant forests, Atmos. Chem. Phys., 15(9), 5145–5159, doi:10.5194/acp-15-5145-2015,

638   2015.

639   Song, M., Liu, P. F., Hanna, S. J., Zaveri, R. A., Potter, K., You, Y., Martin, S. T. and Bertram, A. K.:

640   Relative humidity-dependent viscosity of secondary organic material from toluene photo-oxidation and

641   possible implications for organic particulate matter over megacities, Atmos. Chem. Phys., 16(14),

642   8817–8830, doi:10.5194/acp-16-8817-2016, 2016a.

643   Song, Y. C., Haddrell, A. E., Bzdek, B. R., Reid, J. P., Bannan, T., Topping, D. O., Percival, C. and

644   Cai, C.: Measurements and Predictions of Binary Component Aerosol Particle Viscosity, J. Phys.

645   Chem. A, 120(41), 8123–8137, doi:10.1021/acs.jpca.6b07835, 2016b.

646   Steimer, S. S., Berkemeier, T., Gilgen, A., Krieger, U. K., Peter, T., Shiraiwa, M. and Ammann, M.:

Atmospheric
Measurement
Techniques
Discussions

Open Access

647 Shikimic acid ozonolysis kinetics of the transition from liquid aqueous solution to highly viscous glass,

648 Phys. Chem. Chem. Phys., 17(46), 31101–31109, doi:10.1039/C5CP04544D, 2015.

649 Surratt, J. D., Murphy, S. M., Kroll, J. H., Ng, N. L., Hildebrandt, L., Sorooshian, A., Szmigielski, R.,

650 Vermeylen, R., Maenhaut, W., Claeys, M., Flagan, R. C. and Seinfeld, J. H.: Chemical Composition of

651 Secondary Organic Aerosol Formed from the Photooxidation of Isoprene, J. Phys. Chem. A, 110(31),

652 9665–9690, doi:10.1021/jp061734m, 2006.

653 Surratt, J. D., Chan, A. W. H., Eddingsaas, N. C., Chan, M., Loza, C. L., Kwan, A. J., Hersey, S. P.,

654 Flagan, R. C., Wennberg, P. O. and Seinfeld, J. H.: Reactive intermediates revealed in secondary

655 organic aerosol formation from isoprene, Proc. Natl. Acad. Sci., 107(15), 6640–6645,

656 doi:10.1073/pnas.0911114107, 2010.

657 Vaden, T. D., Imre, D., Beránek, J., Shrivastava, M. and Zelenyuk, A.: Evaporation kinetics and phase

658 of laboratory and ambient secondary organic aerosol, Proc. Natl. Acad. Sci., 108(6), 2190–2195,

659 doi:10.1073/pnas.1013391108, 2011.

660 Virtanen, A., Joutsensaari, J., Koop, T., Kannosto, J., Yli-Pirilä, P., Leskinen, J., Mäkelä, J. M.,

661 Holopainen, J. K., Pöschl, U., Kulmala, M., Worsnop, D. R. and Laaksonen, A.: An amorphous solid

662 state of biogenic secondary organic aerosol particles, Nature, 467(7317), 824–827,

663 doi:10.1038/nature09455, 2010.

664 Virtanen, A., Kannosto, J., Kuuluvainen, H., Arffman, A., Joutsensaari, J., Saukko, E., Hao, L., Yli-

665 Pirilä, P., Tiitta, P. and Holopainen, J. K.: Bounce behavior of freshly nucleated biogenic secondary

666 organic aerosol particles, Atmos. Chem. Phys., 11(16), 8759–8766, doi:10.5194/acp-11-8759-2011,

667 2011.

668 Wang, B., O'Brien, R. E., Kelly, S. T., Shilling, J. E., Moffet, R. C., Gilles, M. K. and Laskin, A.:

669 Reactivity of Liquid and Semisolid Secondary Organic Carbon with Chloride and Nitrate in

670 Atmospheric Aerosols, J. Phys. Chem. A, 119(19), 4498–4508, doi:10.1021/jp510336q, 2015.

671 Wheeler, M. J. and Bertram, A. K.: Deposition nucleation on mineral dust particles: a case against

672 classical nucleation theory with the assumption of a single contact angle, Atmos. Chem. Phys., 12(2),

673 1189–1201, doi:10.5194/acp-12-1189-2012, 2012.

674 Wilson, T. W., Murray, B. J., Wagner, R., Möhler, O., Saathoff, H., Schnaiter, M., Skrotzki, J., Price,

675 H. C., Malkin, T. L. and Dobbie, S.: Glassy aerosols with a range of compositions nucleate ice

676 heterogeneously at cirrus temperatures, Atmos. Chem. Phys., 12(18), 8611–8632, doi:10.5194/acp-12-

Atmospheric
Measurement
Techniques
Discussions

677   8611-2012, 2012.

678   Wong, J. P. S., Zhou, S. and Abbatt, J. P. D.: Changes in Secondary Organic Aerosol Composition and

679   Mass due to Photolysis: Relative Humidity Dependence, J. Phys. Chem. A, 119(19), 4309–4316,

680   doi:10.1021/jp506898c, 2015.

681   Ye, Q., Robinson, E. S., Ding, X., Ye, P., Sullivan, R. C. and Donahue, N. M.: Mixing of secondary

682   organic aerosols versus relative humidity, Proc. Natl. Acad. Sci. , 113(45), 12649–12654,

683   doi:10.1073/pnas.1604536113, 2016.

684   Yeung, M. C., Lee, A. K. Y. and Chan, C. K.: Phase Transition and Hygroscopic Properties of

685   Internally Mixed Ammonium Sulfate and Adipic Acid (AS-AA) Particles by Optical Microscopic

686   Imaging and Raman Spectroscopy, Aerosol Sci. Technol., 43(5), 387–399,

687   doi:10.1080/02786820802672904, 2009.

688   Zaveri, R. A., Easter, R. C., Shilling, J. E. and Seinfeld, J. H.: Modeling kinetic partitioning of

689   secondary organic aerosol and size distribution dynamics: representing effects of volatility, phase state,

690   and particle-phase reaction, Atmos. Chem. Phys., 14(10), 5153–5181, doi:10.5194/acp-14-5153-2014,

691   2014.

692   Zelenyuk, A., Imre, D., Beránek, J., Abramson, E., Wilson, J. and Shrivastava, M.: Synergy between

693   Secondary Organic Aerosols and Long-Range Transport of Polycyclic Aromatic Hydrocarbons,

694   Environ. Sci. Technol., 46(22), 12459–12466, doi:10.1021/es302743z, 2012.

695   Zhang, Q., Jimenez, J. L., Canagaratna, M. R., Allan, J. D., Coe, H., Ulbrich, I., Alfarra, M. R.,

696   Takami, A., Middlebrook, A. M., Sun, Y. L., Dzepina, K., Dunlea, E., Docherty, K., DeCarlo, P. F.,

697   Salcedo, D., Onasch, T., Jayne, J. T., Miyoshi, T., Shimono, A., Hatakeyama, S., Takegawa, N.,

698   Kondo, Y., Schneider, J., Drewnick, F., Borrmann, S., Weimer, S., Demerjian, K., Williams, P.,

699   Bower, K., Bahreini, R., Cottrell, L., Griffin, R. J., Rautiainen, J., Sun, J. Y., Zhang, Y. M. and

700   Worsnop, D. R.: Ubiquity and dominance of oxygenated species in organic aerosols in

701   anthropogenically-influenced Northern Hemisphere midlatitudes, Geophys. Res. Lett., 34(13), L13801,

702   doi:10.1029/2007GL029979, 2007.

703   Zhou, S., Lee, A. K. Y., McWhinney, R. D. and Abbatt, J. P. D.: Burial Effects of Organic Coatings on

704   the Heterogeneous Reactivity of Particle-Borne Benzo[a]pyrene (BaP) toward Ozone, J. Phys. Chem.

705   A, 116(26), 7050–7056, doi:10.1021/jp3030705, 2012.

706   Zobrist, B., Marcolli, C., Pedernera, D. A. and Koop, T.: Do atmospheric aerosols form glasses?,

707   Atmos. Chem. Phys., 8(17), 5221–5244, doi:10.5194/acp-8-5221-2008, 2008.

708

709

Tables

Table 1. The molar masses (M_w) and hydrodynamic radii (R_H) of erythritol and rhodamine B isothiocyanate-dextran (RBID), which are used as the matrix and diffusing fluorescent dye in this work, respectively.
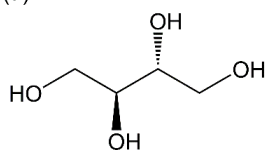
Compound	M_w (g mol^{-1})	R_H (Å)	References
Erythritol	122.12	3.4 ± 0.3	Kiyosawa (1991)
			Schultz and Solomon (1961)
Rhodamine B isothiocyanate-dextran (RBID)	70,000 (on average)	59 ± 1	Floury et al. (2015) Paës et al. (2017)

Figures

(a)

(b)
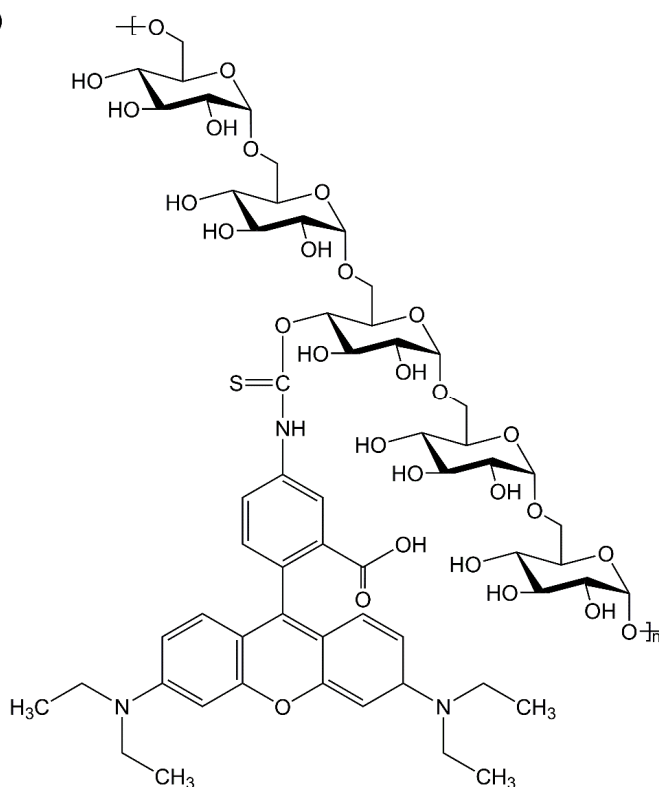
Figure 1. Molecular structures of (a) erythritol and (b) rhodamine B isothiocyanate – dextran (RBID)
in neutral form. On average, n ≈ 429.

Atmospheric
Measurement
Techniques
Discussions

Open Access
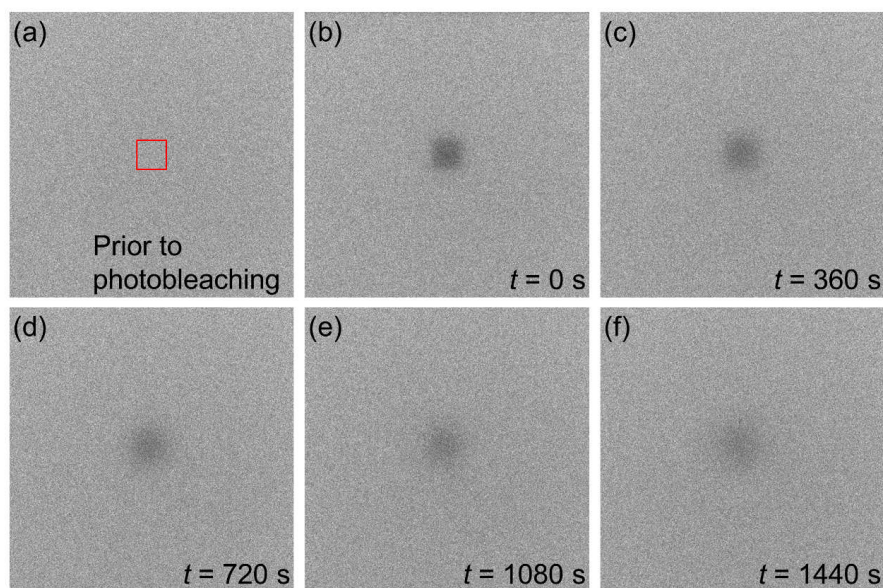
Figure 2. Images captured during an rFRAP experiment for erythritol-water thin films conditioned at $a_w = 0.023 \pm 0.023$. RBID concentration in the films was approximately 0.3 weight percent. The red square in (a) indicates the region selected for photobleaching. Images (b–f) were recorded at 0, 360, 720, 1080 and 1440 s after photobleaching. Dimensions of the images and the red square are $60 \times 60 \ \mu m^2$ and $6 \times 6 \ \mu m^2$, respectively.

730
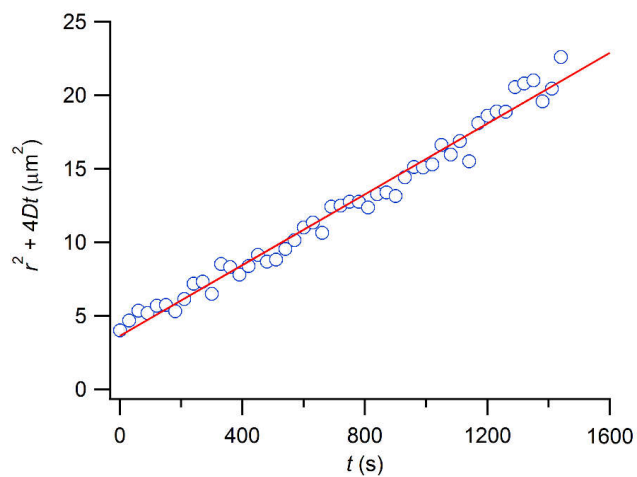
Figure 3. $r^2 + 4Dt$ as a function of t for the diffusion of RBID in erythritol-water matrix with a_w =

732   0.023 ± 0.023. RBID concentration in the conditioned films was approximately 0.3 weight percent.

733   The red line represents a linear fit to the data.

734

Atmospheric
Measurement
Techniques
Discussions

Open Access

735
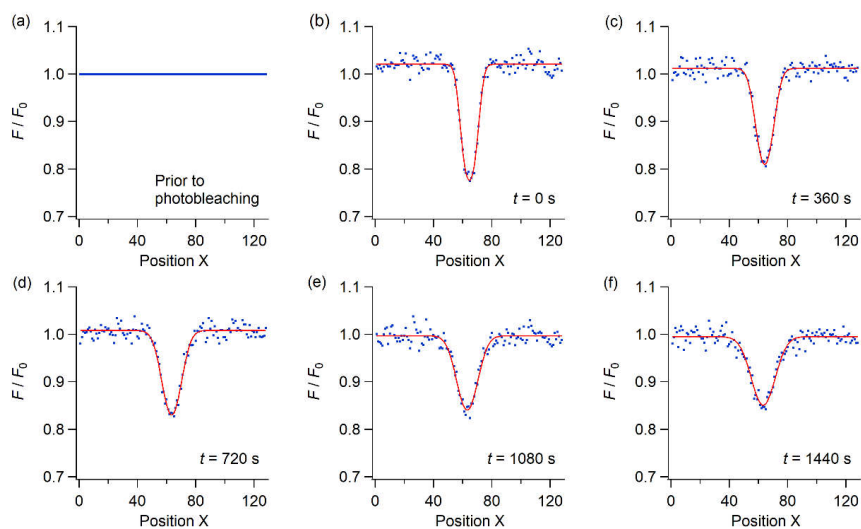
Figure 4. Cross-sectional view of the normalized fluorescence intensities (F / F_0) along the x-axis

736 during an rFRAP experiment. Blue dots correspond to the measured data, while the red lines

737 represent fits to the experimental data using Eq. (2). The sample films were conditioned at a_w =

738 0.023 ± 0.023. RBID concentration in the conditioned films was approximately 0.3 weight percent.

739 Panel (a) shows the cross-section prior to photobleaching. F / F_0 equals 1 because the image was

740 normalized against itself. Panels (b–f) show the cross-sections at 0, 360, 720, 1080 and 1440 s after

741 photobleaching, corresponding to frames (b–f) in Fig. 2.

742

743

744
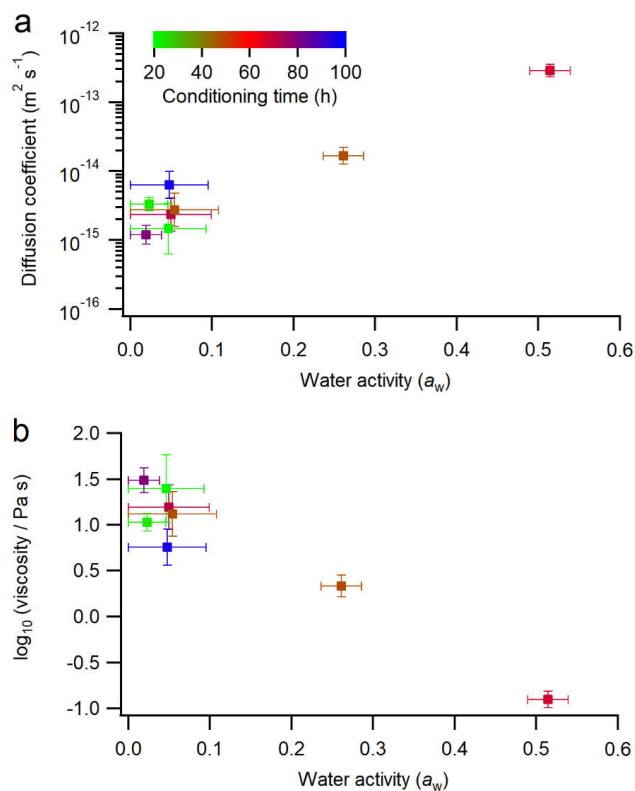
Figure 5. (a) The measured diffusion coefficients of RBID as a function of a_w. (b) The viscosity of

erythritol-water particles as a function of a_w based on the measured RBID diffusion coefficients and

the Stokes-Einstein equation. Results from rFRAP measurements are color-coded by the sample

conditioning time prior to the rFRAP experiments. The color scale applies to both panel (a) and (b).

Horizontal error bars indicate the upper and lower limits of a_w. Vertical error bars correspond to two

standard deviations of diffusion coefficient (in panel a) and $\log_{10}$ (viscosity / Pa s) (in panel b).

751
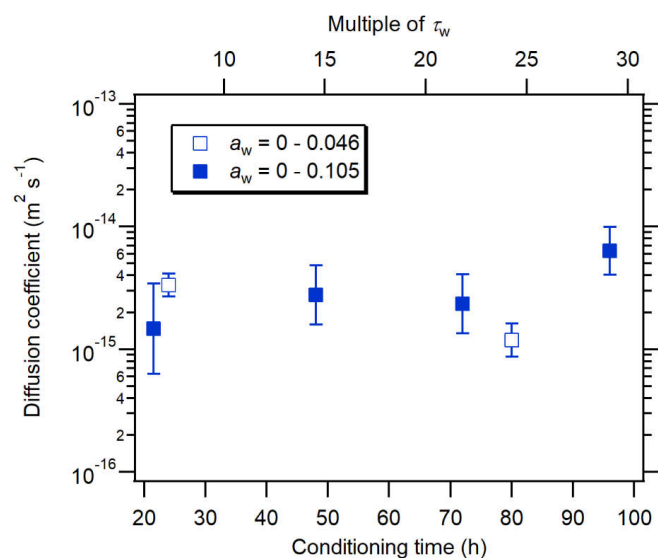
Figure 6. The diffusion coefficient of RBID as a function of the time allowed for conditioning erythritol-water particles at $a_w = 0 - 0.046$ (open squares) and $0 - 0.105$ (filled squares). The secondary (top) x-axis represents the conditioning time expressed in multiples of τ_w (characteristic time for the diffusion of water molecules within the erythritol-water droplets). For the calculation of τ_w, the lower limit of a_w (i.e., 0) was taken, leading to maximum τ_w values of 3.3 h for droplets with a radius of 100 μm. Error bars represent two standard deviations of RBID diffusion coefficients.
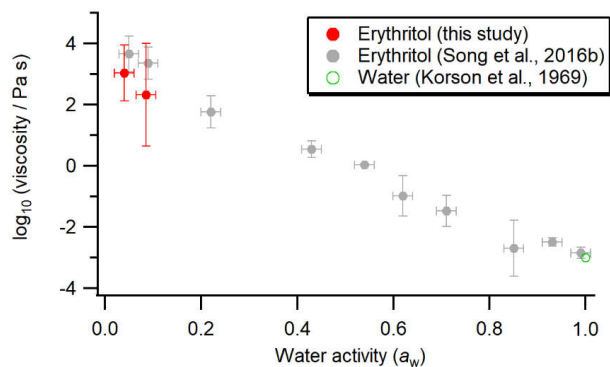
Figure 7. Viscosity of erythritol-water particles (on a $\log_{10}$ scale) as a function of a_w, determined using the aerosol optical tweezer technique. Red circles represent experimental results from this study. Gray circles represent experimental results from Song et al. (2016b). The green circle represents the viscosity of pure water at 293 K (Korson et al., 1969). Horizontal error bars (± 0.02) indicate the upper and lower limits of a_w. Vertical error bars represent two standard deviations of $\log_{10}$ (viscosity / Pa s).
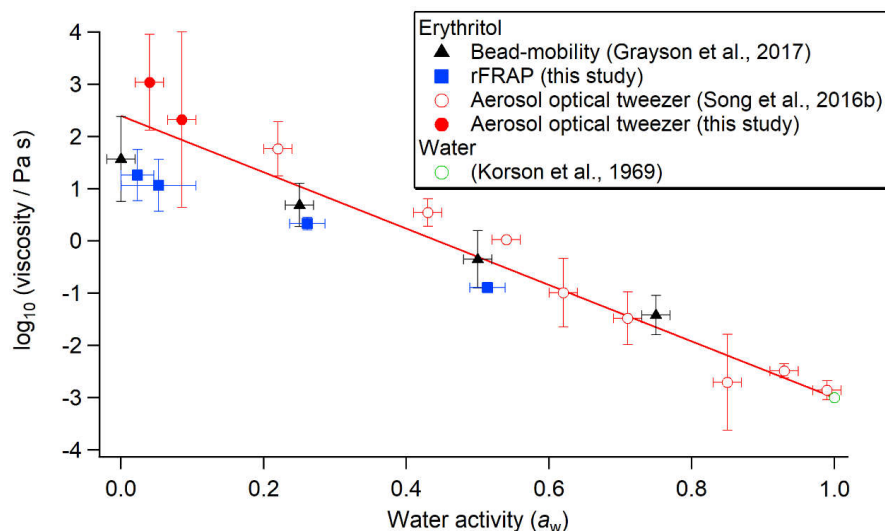
Figure 8. Viscosity of erythritol-water particles as a function of a_w measured by the bead-mobility technique (black triangles) (Grayson et al., 2017), the rFRAP technique (blue squares) and the aerosol optical tweezer technique (open red circles – from Song et al. (2016b), solid red circles – this study). The viscosity of pure water at 293 K (open green circle) (Korson et al., 1969) is also included for comparison. Horizontal error bars ($\pm$ 0.02) indicate the upper and lower limits of a_w. Vertical error bars represent two standard deviations of $\log_{10}$ (viscosity / Pa s). The red line is a linear fit to the data shown in the plot using the orthogonal distance regression-fitting algorithm, which is weighted based on the uncertainty in viscosity data. The equation of the linear fit is $\log_{10}$ (viscosity / Pa s) = (2.393 $\pm$ 0.246) + (–0.054 $\pm$ 0.002) $\cdot$ (100 a_w). Uncertainties in the slope and y-axis intercept correspond to two standard deviations.

Atmospheric
Measurement
Techniques
Discussions
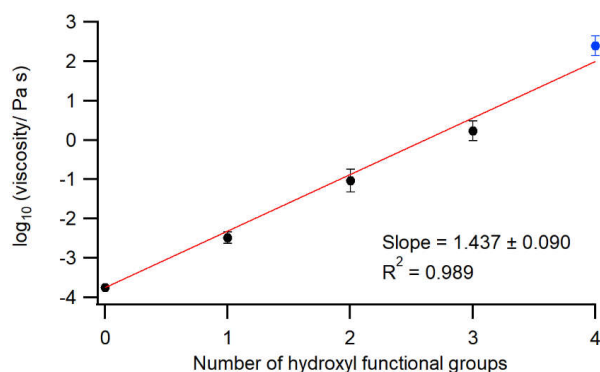
Figure 9. Viscosities of compounds with a linear C_4 carbon backbone at 292 – 295 K on a log_{10} scale plotted against the number of OH functional groups. Black circles represent viscosities of the compounds with 0 – 3 OH functional groups (i.e., n-butane, 1-butanol, 2-butanol, 1,2-butanediol, 1,4-butanediol, 2,3-butanediol, 1,2,3-butanetriol and 1,2,4-butanetriol) taken from literature (Grayson et al., 2017; Rothfuss and Petters, 2017; Song et al., 2016b). For the literature data points, the error bars are two standard deviations of log_{10} (viscosity / Pa s) of multiple compounds. The blue circle represents the viscosity of pure erythritol, with error bars of two standard deviations, based on the linear fit in Fig. 8. The red line is a linear fit to the data, which is weighted based on the uncertainties in viscosity data. The slope and regression coefficient (R^2) are shown in the annotation. The uncertainty in the slope corresponds to two standard deviations.
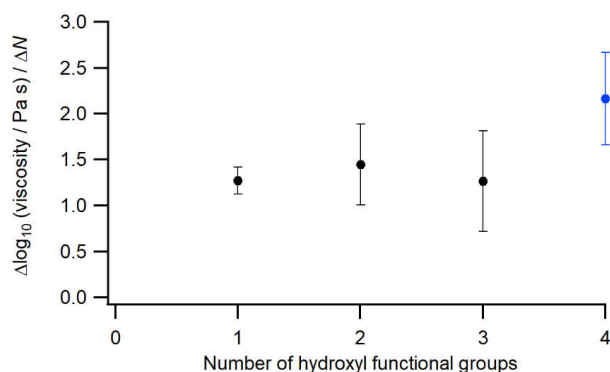
Figure 10. The viscosity sensitivity parameter at 292 – 295 K plotted against the number of OH functional groups for linear C_4 compounds (alkane, alcohol and polyols). Black circles represent values estimated using literature data alone (Grayson et al., 2017; Rothfuss and Petters, 2017; Song et al., 2016b); the blue circle represents the value estimated using experimental results from this work and literature data (Grayson et al., 2017; Song et al., 2016b). The error bars are propagated from the uncertainties shown in Fig. 9.